

Deep MAGSAC++

Wei Tong¹, Jiri Matas³, and Daniel Barath²

¹ Faculty of Informatics, Eotvos Lorand University, ² Department of Computer Science, ETH Zurich

³ VRG, Faculty of Electrical Engineering, Czech Technical University in Prague

weitong@student.elte.hu, matas@cmp.felk.cvut.cz, danielbela.barath@inf.ethz.ch

Abstract

We propose *Deep MAGSAC++* combining the advantages of traditional and deep robust estimators. We introduce a novel loss function that exploits the orientation and scale from partially affine covariant features, e.g., *SIFT*, in a geometrically justifiable manner. The new loss helps in learning higher-order information about the underlying scene geometry. Moreover, we propose a new sampler for RANSAC that always selects the sample with the highest probability of consisting only of inliers. After every unsuccessful iteration, the probabilities are updated in a principled way via a Bayesian approach. The prediction of the deep network is exploited as prior inside the sampler. Benefiting from the new loss, the proposed sampler and a number of technical advancements, *Deep MAGSAC++* is superior to the state-of-the-art both in terms of accuracy and runtime on thousands of image pairs from publicly available datasets for essential and fundamental matrix estimation.

1. Introduction

The RANSAC (RANdom Sample Consensus) algorithm proposed by Fischler and Bolles [17] in 1981 has become the most widely used robust estimator in computer vision. RANSAC and its variants have been successfully applied in a wide range of vision applications, e.g., short baseline stereo [45, 47], wide baseline matching [29, 31, 34], to perform [8, 54] or initialize multi-model fitting algorithms [24, 33], image mosaicing [20], pose-graph initialization for SfM pipelines [40, 41], motion segmentation [45]. Briefly, RANSAC repeatedly selects random minimal subsets of the data points, and fits a model, e.g., a 3D plane to three points or an essential matrix to five 2D point correspondences. The quality of the model is then measured, for instance, as the cardinality of its support, i.e., the number of data points closer than a manually set inlier-outlier threshold. Finally, the model with the highest quality, polished, e.g., by least-squares fitting on all inliers, is returned.

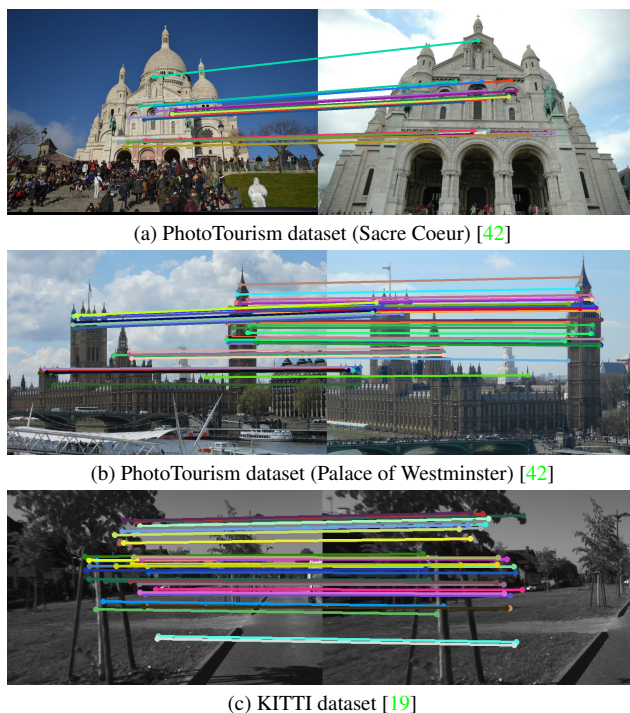


Figure 1. Example image pairs used for estimating essential and fundamental matrices with point correspondences drawn.

Since the publication of RANSAC, a number of modifications have been proposed replacing components of the original algorithm. To improve the accuracy by better modelling the noise in the data, different model quality calculation techniques have been investigated. For instance, MLE-SAC [46] estimates the quality by a maximum likelihood procedure with all its beneficial properties. In MSAC [46], the loss is formulated as a truncated quadratic error by assigning constant loss to the outliers (i.e., points with residuals larger than the inlier-outlier threshold) and a quadratic one to the inliers. In the recently proposed MAGSAC++ [9], the model quality calculation is formulated as a marginalization over a range of noise scales. It allows MAGSAC++

to be significantly less sensitive to the inlier-outlier threshold than other robust estimators. According to a recent survey [27], MAGSAC++ is currently the most accurate robust estimator. In this paper, we focus on combining MAGSAC++ with a deep learning approach trained on a new loss and combined with a new sampler.

Improving the sampler accelerates the robust estimation procedure via selecting a good sample early and, thus, triggering the termination criterion. The NAPSAC [44] sampler assumes that inliers are spatially coherent and, thus, it draws samples from a hyper-sphere centered at the first, randomly selected, location-defining point. The GroupSAC algorithm [32] assumes that inliers are often “similar” and, thus, can be separated into groups. PROSAC [15] exploits an a priori predicted inlier probability rank of each point and starts the sampling with the most promising ones. Progressively, samples that are less likely to lead to the sought model are drawn. The sampler used in [14] assumes that we are given prior knowledge, *e.g.*, from a deep network, about the inlier probability of each point. It selects samples according to the probability assuming that it follows a categorical distribution over the discrete set of observations.

Recently, several algorithms were proposed approaching the robust relative pose estimation problem using neural networks. Context normalization networks [50] is the first paper on the topic which proposes to use PointNet (MLP) with batch normalization [23] as context mechanism. Attentive context normalization networks [43] introduces a special architectural block for the task. Deep Fundamental matrix estimation [35] uses differentiable iteratively re-weighted least-squares with predicted weights. The OANet algorithm [52] introduces several architectural blocks for the correspondence filtering. Neural Guided RANSAC [14] uses a CNe-like architecture with a different training objective. The predicted correspondence scores are exploited inside RANSAC by using a guided sampling algorithm that helps in finding accurate models early. CLNet [53] introduces several algorithmic and architectural improvements to first remove gross outliers with iterative pruning. These techniques, in general, provide alternatives for tentative correspondence pre-filtering and weighting. However, they do not replace standard robust estimation as it is shown in [4].

This paper has three main contributions. First, we focus on combining two state-of-the-art algorithms, *i.e.*, MAGSAC++ [9] and NG-RANSAC [14], in order to improve the relative pose accuracy on a wide range of scenes. Second, we propose a way of incorporating the orientation and scale from, *e.g.*, SIFT features, in a geometrically meaningful manner directly in the loss function minimized during training. The new loss leads to more accurate results than simply using pose or epipolar errors. Third, we propose a new sampler that exploits the predicted inlier probabilities in a more effective way than [14, 15]. The new sam-

pler leads to the best results even with the SNN [26] ratio, without any neural network applied.

2. Deep MAGSAC++

The MAGSAC++ algorithm [10] formulates the robust estimation problem as an iteratively re-weighted least-squares (IRLS) approach. Both the model quality calculation and inlier selection are done without making strict inlier-outlier decisions. The model parameters θ_{i+1} in the $(i + 1)$ th step of the IRLS are calculated as follows:

$$\theta_{i+1} = \arg \min_{\theta} \sum_{\mathbf{p} \in \mathcal{P}} w(R(\theta_i, \mathbf{p})) R^2(\theta, \mathbf{p}), \quad (1)$$

where the weight of point \mathbf{p} is

$$w(R(\theta_i, \mathbf{p})) = \int_0^{+\infty} \mathbf{P}(\mathbf{p} \mid \theta_i, \sigma) f(\sigma) d\sigma \quad (2)$$

and $\theta_0 = \theta$, *i.e.*, the initial model from the minimal sample.

The inlier residuals are assumed to be corrupted by Gaussian noise and, thus, have χ -distribution. The noise standard deviation σ is assumed to be uniformly distributed within interval $(0, \sigma_{\max})$. The weight function defined in (2) is the marginal density of the inlier residuals as follows:

$$w(r) = \int_0^{+\infty} g(r \mid \sigma) f(\sigma) d\sigma. \quad (3)$$

Let $\tau(\sigma) = k\sigma$ be the chosen quantile of the χ -distribution. For residual $0 \leq r \leq k\sigma_{\max}$,

$$w(r) = \frac{1}{\sigma_{\max}} \int_{r/k}^{\sigma_{\max}} g(r \mid \sigma) d\sigma = \frac{1}{\sigma_{\max}} C(\nu) 2^{\frac{\nu-1}{2}} \left(\Gamma\left(\frac{\nu-1}{2}, \frac{r^2}{2\sigma_{\max}^2}\right) - \Gamma\left(\frac{\nu-1}{2}, \frac{k^2}{2}\right) \right)$$

and, for $r > k\sigma_{\max}$, weight $w(r) = 0$. Function

$$\Gamma(a, x) = \int_x^{+\infty} t^{a-1} \exp(-t) dt$$

is the upper incomplete gamma function. Due to the design choices, weight $w(r)$ is positive and decreasing on interval $[0, \tau(\sigma_{\max})]$. Thus there is a ρ -function of an M-estimator which is minimized by IRLS using $w(r)$ and each iteration guarantees a non-increase in its loss function (chapter 9 of [28]). Consequently, it converges to a local minimum.

IRLS (1) where $w(r)$ is defined by (3) with $\tau(\sigma) = 3.64\sigma$, where 3.64 is the 0.99 quantile of the χ -distribution with $\nu = 4$, is called σ -consensus++ for problems using point correspondences. Parameter σ_{\max} is a user-defined maximum noise level parameter. The σ -consensus++ algorithm is applied for fitting to a non-minimal sample and,

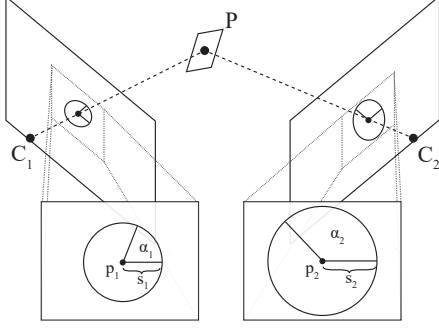


Figure 2. Visualization of the orientation- and scale-covariant features. Point \mathbf{P} and the surrounding patch projected into cameras \mathbf{C}_1 and \mathbf{C}_2 . A window showing the projected points $\mathbf{p}_1 = [u_1 \ v_1 \ 1]^T$ and $\mathbf{p}_2 = [u_2 \ v_2 \ 1]^T$ are cut out and enlarged. The rotation of the feature in the i th image is α_i and the size is s_i ($i \in \{1, 2\}$). The scaling from the 1st to the 2nd image is calculated as $s = s_2/s_1$.

also, as a post-processing to improve the output of any robust estimator. In order to combine MAGSAC++ with recent neural network-based techniques, we adopt the Neural Guided RANSAC (NG-RANSAC) architecture [14]. The NG-RANSAC algorithm predicts the probability of each point correspondence being inlier and uses a weighted sampling approach to incorporate this information in the robust estimation procedure. Due to the neural network and the robust estimator being loosely connected in such a manner, the robust estimator can be replaced by MAGSAC++. While training the weights with sparse correspondences end-to-end, the inlier masks and selected samples are utilized to update the gradients of the neurons and generate the point probabilities as the weights for the consequent epochs. We use additional side information as well, namely, the scale and orientation of each SIFT feature.

In the next sections, we focus on improving the network by considering new geometry-induced loss functions and, also, propose a new sampler that better exploits the predicted probabilities than the importance sampler from [14] and PROSAC proposed by Chum *et al.* [15].

3. Scale and Orientation Loss

We propose a loss function considering that, in most of the two-view cases, we apply feature detectors that provide more information about the underlying scene geometry than simply the point coordinates. For instance, ORB [39] features contain the orientation of the image patches centered on the detected points in the two images. In addition to the feature orientation, the SIFT [26] and SURF [13] detectors return a uniform scaling parameter. Even the full affine warping of the patch can be recovered when using affine-covariant feature detectors, *e.g.*, Hessian-Affine [30] or MODS [31]. The point correspondence and the affine warp is the so-called affine correspondence.

To the best of our knowledge, the plus information that such features provide have not yet been exploited in a geometrically meaningful manner in the loss minimized during the training. Recent deep networks, *e.g.*, [14], only use it as a side information added to the learned feature vectors.

3.1. Affine Epipolar Error

In order to interpret fully or partially affine-covariant features, we adopt the definition from [5] and the affine transformation model from [3]. We consider an affine correspondence (AC) a triplet: $(\mathbf{p}_1, \mathbf{p}_2, \mathbf{A})$, where $\mathbf{p}_1 = [u_1 \ v_1 \ 1]^T$ and $\mathbf{p}_2 = [u_2 \ v_2 \ 1]^T$ are a corresponding homogeneous point pair in the two images, and

$$\mathbf{A} = \begin{bmatrix} a_1 & a_2 \\ a_3 & a_4 \end{bmatrix} = \begin{bmatrix} \cos(\alpha) & -\sin(\alpha) \\ \sin(\alpha) & \cos(\alpha) \end{bmatrix} \begin{bmatrix} s_u & w \\ 0 & s_v \end{bmatrix}, \quad (4)$$

is a 2×2 linear transformation describing the relationship of the infinitesimal image patches centered on points \mathbf{p}_1 and \mathbf{p}_2 , where α is rotation, s_u and s_v are the scales along the axes, and w is the shear parameter. Formally, \mathbf{A} is defined as the first-order Taylor-approximation of the $3D \rightarrow 2D$ projection functions. For perspective cameras, \mathbf{A} is the first-order approximation of the related 3×3 homography.

The relationship of affine correspondences and epipolar geometry is shown in [5, 36] with [5] providing a geometrically interpretable definition of the constraint as

$$\mathbf{A}^{-T} \mathbf{n}_1 = -\mathbf{n}_2 \quad (5)$$

where $\mathbf{n}_1 = (\mathbf{F}^T \mathbf{p}_2)_{[1:2]}$ and $\mathbf{n}_2 = (\mathbf{F} \mathbf{p}_1)_{[1:2]}$ are the normals of the epipolar lines in the two images, and lower-index $\mathbf{v}_{[1:2]}$ selects the first two coordinates of a vector \mathbf{v} .

While constraint (5) is originally formulated as two linear equations in [5] to simplify the estimation, it can be rewritten to two geometrically meaningful constraints that we can use in the loss function. First, (5) implies that \mathbf{A}^{-T} rotates the normal in the first image to its corresponding pair in the second one as $(\mathbf{A}^{-T} \mathbf{n}_1) \times \mathbf{n}_2 = 0$, where the angle between $\mathbf{A}^{-T} \mathbf{n}_1$ and \mathbf{n}_2 can be used as an error for an estimated fundamental matrix $\hat{\mathbf{F}}$ as follows:

$$f(\mathbf{A}, \hat{\mathbf{F}}, \mathbf{p}_1, \mathbf{p}_2) = \cos^{-1} \frac{(\mathbf{A}^{-T} (\hat{\mathbf{F}}^T \mathbf{p}_2)_{[1:2]}) (\hat{\mathbf{F}} \mathbf{p}_1)_{[1:2]}}{\|(\hat{\mathbf{F}}^T \mathbf{p}_2)_{[1:2]}\| \|(\hat{\mathbf{F}} \mathbf{p}_1)_{[1:2]}\|}. \quad (6)$$

Second, (5) implies that the scale change is

$$\det \mathbf{A} = \frac{|\mathbf{n}_2|}{|\mathbf{n}_1|} = \frac{|\mathbf{F} \mathbf{p}_1|_{[1:2]}}{|(\mathbf{F}^T \mathbf{p}_2)_{[1:2]}} \quad (7)$$

providing another geometrically meaningful error as

$$g(\mathbf{A}, \hat{\mathbf{F}}, \mathbf{p}_1, \mathbf{p}_2) = \det \mathbf{A} - \frac{|\mathbf{F} \mathbf{p}_1|_{[1:2]}}{|(\hat{\mathbf{F}}^T \mathbf{p}_2)_{[1:2]}}. \quad (8)$$

These errors can be used to measure the quality of a fundamental or essential matrix given an affine correspondence.

3.2. Affine Loss Function

In practice, we usually are given partially affine-covariant features, *e.g.*, SIFT, that do not allow using error functions (6) and (8) directly. In order to define a justifiable loss, we first approximate the local affine transformation $\hat{\mathbf{A}}$ using the rotations α_1, α_2 and scales s_1, s_2 from the SIFT features via the affine transformation model in (4) assuming that shear $w = 0$, rotation $\alpha = \alpha_2 - \alpha_1$, and $s_u = s_v = s_2/s_1$ is a uniform scaling along the axes similarly as in [3], see Fig. 2. It is important to note that directly using $\hat{\mathbf{A}}$ to measure the error of the prediction is still not viable since $\hat{\mathbf{A}}$ is only an approximation and, thus, (6) and (8) are not zero even if the ground truth fundamental matrix is used. We, therefore, define our orientation loss as

$$L_{\text{ori}}(\dots) = \left| f(\hat{\mathbf{A}}, \hat{\mathbf{F}}, \mathbf{p}_1, \mathbf{p}_2) - f(\hat{\mathbf{A}}, \mathbf{F}, \mathbf{p}_1, \mathbf{p}_2) \right|, \quad (9)$$

and the scale loss as

$$L_{\text{scale}}(\dots) = \left| g(\hat{\mathbf{A}}, \hat{\mathbf{F}}, \mathbf{p}_1, \mathbf{p}_2) - g(\hat{\mathbf{A}}, \mathbf{F}, \mathbf{p}_1, \mathbf{p}_2) \right|, \quad (10)$$

where \mathbf{F} is the ground truth fundamental matrix used as a target for the network and $\hat{\mathbf{F}}$ is the prediction. It can be easily seen that measuring the error in this way allows to ignore the approximative nature of $\hat{\mathbf{A}}$.

The final loss minimized when training the network is

$$L(\mathbf{F}, \hat{\mathbf{F}}, \mathcal{P}) = \sum_{(\mathbf{p}_1, \mathbf{p}_2, \hat{\mathbf{A}}) \in \mathcal{P}} w_{\text{ori}} L_{\text{ori}}(\mathbf{F}, \hat{\mathbf{F}}, \hat{\mathbf{A}}, \mathbf{p}_1, \mathbf{p}_2) + w_{\text{scale}} L_{\text{scale}}(\mathbf{F}, \hat{\mathbf{F}}, \hat{\mathbf{A}}, \mathbf{p}_1, \mathbf{p}_2) + \dots$$

where $\mathcal{P} = \{(\mathbf{p}_1, \mathbf{p}_2, \alpha_1, \alpha_2, s_1, s_2) \mid \mathbf{p}_1, \mathbf{p}_2 \in \mathbb{R}^2 \wedge \alpha_1, \alpha_2 \in [0, 2\pi] \wedge s_1, s_2 \in \mathbb{R}^+\}$ is the set of SIFT correspondences, w_{ori} and w_{scale} are weighting parameters, and \dots represents other frequently used error metrics, *e.g.*, epipolar or pose error, or inlier number.

4. Adaptive Re-ordering Sampler

In this section, we describe a new sampler that always selects the sample with the highest probability of containing only inliers. This probability is updated adaptively during the robust estimation procedure. The new sampler will be called **AR-Sampler** in the remainder of the paper.

Let us assume that we are given point correspondences $p_{i_1^t}, p_{i_2^t}, \dots, p_{i_n^t} \in \mathcal{P}$ with inlier probabilities $\mu_{i_1^t}, \mu_{i_2^t}, \dots, \mu_{i_n^t} \in [0, 1]$ such that $\mu_{i_1^t} \geq \mu_{i_2^t} \geq \dots \geq \mu_{i_n^t}$, where $i_1^t, \dots, i_n^t \in [1, n]$ are indices in the t th RANSAC iteration ensuring that the points are ordered by the inlier probabilities in a descending order. The probability of sample $S = (p_{j_1}, p_{j_2}, \dots, p_{j_m}) \in \mathcal{P}^\times$ consisting only of inliers is calculated as $\mu_S = \prod_{k=1}^m \mu_{j_k}$, where m is the sample size, *e.g.*, $m = 5$ for essential matrix estimation. Consequently,

Algorithm 1 Probability Update.

Input: p_1, \dots, p_n – points; μ_1, \dots, μ_n – probabilities
 S – minimal sample; N_1, \dots, N_n – usage numbers
 $(a_1, b_1), \dots, (a_n, b_n)$ – initial distr. parameters
Output: μ'_1, \dots, μ'_n – updated inlier probabilities

```

1: for  $i \in [1, n]$  do
2:   if  $p_i \in S$  then ▷ Update  $\mu$  in the sample
3:      $a'_i \leftarrow a_i; b'_i \leftarrow b_i + N_i$ 
4:      $\mu'_i \leftarrow a'_i / (a'_i + b'_i)$ 
5:   else ▷ Other point have the same  $\mu$  as before
6:      $\mu'_i \leftarrow \mu_i$ 

```

Algorithm 2 Adaptive Re-ordering Sampler.

Input: p_1, \dots, p_n – points; μ_1, \dots, μ_n – inlier probs.
 m – sample size; N_1, \dots, N_n – usage numbers
 $(a_1, b_1), \dots, (a_n, b_n)$ – initial distr. parameters
Output: S^* – minimal sample

```

1:  $i_1, \dots, i_n \leftarrow \text{sort}(\mu_1, \dots, \mu_n)$  ▷ Sorted indices
2:  $S^* \leftarrow \{p_{i_j} \mid j \in [1, m]\}$  ▷ Points with highest  $\mu$ 
3: for  $p_{i_j} \in S^*$  do
4:    $N_{i_j} \leftarrow N_{i_j} + 1$  ▷ Increase the usage number
5:    $\mu_{i_j} \leftarrow \text{Update}(a_{i_j}, b_{i_j}, \mu_{i_j}, N_{i_j})$  ▷ Alg. 1

```

the optimal sampler maximizing the sample probability of $S_t^* = (p_{i_1^t}, p_{i_2^t}, \dots, p_{i_m^t})$ in the t th iteration.

In theory, every unsuccessful RANSAC iteration reduces the inlier probability of the points in the minimal sample. In order to model this in a principled way, we update the probabilities using the Bayesian approach after each RANSAC iteration. As prior knowledge, we can either consider the output of the deep network or even the point ordering that the standard second nearest neighbor (SNN) ratio [26] implies. In each update, only the points from the current minimal sample are considered and, thus, the probability of other points remain unchanged in the $t + 1$ -th iteration as we did not gather additional information about them.

In RANSAC, it is assumed that if a sample contains at least a single outlier, it does not lead to the sought model parameters and $\mu_S = \prod_{k=1}^m \mu_{j_k} = 0$. Due to not having individual information about each point in S , the probability of each is reduced proportionally to its prior confidence, *i.e.* the probability it was correct before the sample was drawn, updating μ_j using the Bayesian approach.

The inlier probability of a point correspondence p that has already been selected n_p times during the robust estimation follows the binomial distribution with parameters $\mu_p(n_p)$ and n_p . The usual conjugate prior for a binomial distribution is a beta distribution with prior hyper-parameters $a(n_p)$ and $b(n_p)$, with expectation

Dataset / Method	LMEDS [38]	RSC [18]	GC-RSC [7]	MSC [11]	MSC++ [9]	EAS [16]	NG-RSC [14]	Deep MAGSAC++
Avg. time (ms)	26.67	88.08	175.10	239.41	113.41	317.50	79.75	33.92
Buckingham Palace	0.19	0.20	0.20	0.27	0.26	0.09	0.28	0.33
Brandenburg Gate	0.34	0.42	0.48	0.53	0.54	0.29	0.55	0.61
Colosseum Exterior	0.25	0.25	0.27	0.32	0.31	0.13	0.32	0.36
Grand Place Brussels	0.14	0.14	0.17	0.22	0.21	0.06	0.22	0.32
Notre Dame Front Facade	0.24	0.27	0.38	0.40	0.41	0.13	0.34	0.49
Palace of Westminster	0.19	0.31	0.36	0.37	0.37	0.20	0.38	0.43
Pantheon Exterior	0.49	0.41	0.48	0.62	0.62	0.20	0.62	0.72
Prague Old Town Square	0.10	0.11	0.12	0.16	0.16	0.07	0.17	0.20
Sacre Coeur	0.52	0.64	0.68	0.71	0.71	0.55	0.63	0.75
Taj Mahal	0.36	0.48	0.52	0.52	0.55	0.37	0.55	0.67
Trevi Fountain	0.28	0.29	0.30	0.37	0.35	0.17	0.38	0.43
Westminster Abbey	0.46	0.36	0.49	0.51	0.51	0.20	0.49	0.70
Avg. over all scenes	0.30	0.32	0.37	0.42	0.42	0.21	0.41	0.50

Table 1. Essential matrix estimation on scenes from the PhotoTourism dataset [42]. We report the AUC scores [51] at 10° (higher is better) calculated from the pose error, *i.e.*, the maximum of the relative rotation and translation errors in degrees. The first row shows the average run-times (in milliseconds). The last one reports the scores averaged over all scenes. For RANSAC (RSC), GC-RANSAC (GC-RSC), MAGSAC (MSC) and MAGSAC++ (MSC++), we use the inlier-outlier threshold tuned in [12]. For EAS and NG-RANSAC (NG-RSC), we use the threshold provided by authors. We tuned the threshold for Deep MAGSAC++ on the training set to maximize the accuracy.

$a(n_p)/(a(n_p) + b(n_p))$, and variance

$$v = \frac{a(n_p)b(n_p)}{(a(n_p) + b(n_p))^2(a(n_p) + b(n_p) + 1)}, \quad (11)$$

and posterior hyper-parameters $a(n_p)$ and $b(n_p)$. The posterior distribution parameters are $a(n_p + 1) = a(n_p)$, $b(n_p + 1) = b(n_p) + 1$. The best estimator for $\mu_p(n_p + 1)$ using a quadratic loss function is an expectation of the posterior distribution. Consequently, we set

$$\mu_p(n_p + 1) = \frac{a(n_p + 1)}{a(n_p + 1) + b(n_p + 1)}. \quad (12)$$

For each point correspondence p , the initial parameters of the beta distribution $a(1)$ and $b(1)$ are set using the predicted inlier ratio $\mu_p(1) = \mu_p^1$. We assume that the inlier probability prediction procedure provides the expectation of the prior beta distribution and with the same mean precision for all image pairs. Therefore, the variance v of all these initial beta distributions is equal and can be learned in advance. Given the learned variance, equations

$$\mu_p(1) = \frac{a(1)}{a(1) + b(1)}, \quad (13)$$

$$v = \frac{a(1)b(1)}{(a(1) + b(1))^2(a(1) + b(1) + 1)} \quad (14)$$

lead to

$$a(1) = \frac{(\mu_p(1))^2(1 - \mu_p(1))}{v} - \mu_p(1), \quad (15)$$

$$b(1) = a(1) \frac{1 - \mu_p(1)}{\mu_p(1)}. \quad (16)$$

Parameters $a(1)$ and $b(1)$ are calculated prior to the robust estimation procedure. The sampler and the probability update are shown, respectively, in Algorithms 2 and 1. Both methods contain only a few calculations and, thus, are very efficient. This is expected from a sampler in a RANSAC-like robust estimator where it runs in every iteration. Note that we found that the sampler works better if the probabilities are shuffled by adding a small random number ϵ . Setting ϵ so it is uniformly distributed in-between -0.0005 and 0.0005 works well in our experiments.

5. Experimental Results

This section evaluates the accuracy and speed of Deep MAGSAC++ and the impact of each individual improvements proposed in this paper, *e.g.*, AR-Sampler and affine loss. The compared methods are the OpenCV implementation of RANSAC [17] and LMEDS [37], the implementations provided by the authors of GC-RANSAC [7], MAGSAC [11] and MAGSAC++ [9], NG-RANSAC [14], and the recently published EAS [16] algorithms. Note that

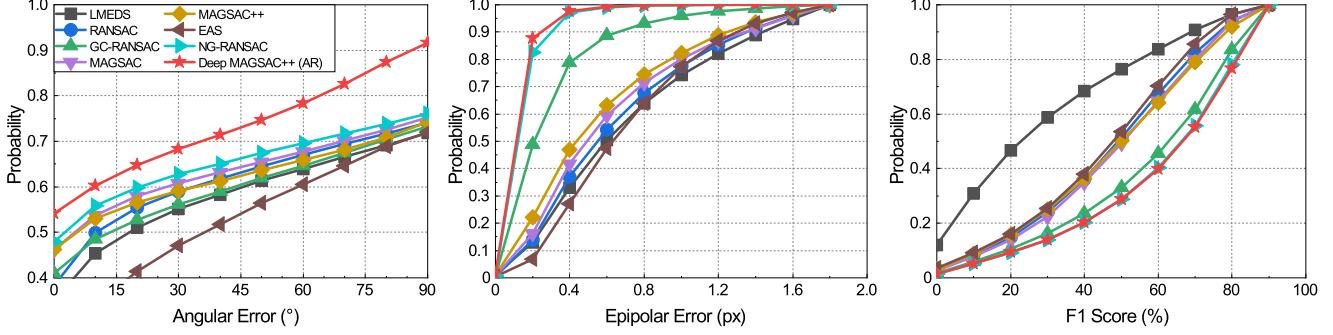


Figure 3. The cumulative distribution functions (CDF) of the angular errors (left) for \mathbf{E} estimation; epipolar errors (middle; in pixels) and F1 score (right; in percentages) for \mathbf{F} estimation. Essential matrix estimation is tested on 12 000 image pairs from the PhotoTourism dataset [42]. Fundamental matrix estimation is evaluated on 9690 pairs from the KITTI benchmark [19]. We use the threshold tuned in [12] for RANSAC, GC-RANSAC, MAGSAC and MAGSAC++. For EAS and NG-RANSAC, we use the ones provided by the authors. In the left two plots, being close to the top-left corner indicates accurate results. In the right one (F1 score), the bottom-right corner is preferable.

we ran CLNet [53] using the model provided by the authors. However, its results were inaccurate and, thus, we do not report them. Our training attempts were unsuccessful.

All the experiments were conducted on Ubuntu 20.04 with GTX 3090Ti, OpenCV 4.5/3.4, and PyTorch 1.7.

Technical details. We use RootSIFT [2] features to improve the estimation accuracy and help the deep network to learn accurate weights. RootSIFT is a strategy normalizing the SIFT [26] descriptors, thus, helping the feature matcher to find good tentative correspondences. When training, we provide the network with the feature scales and orientations as a learned side-information as well. Also, we do SNN ratio [26] filtering on the correspondences as preliminary step. In the SNN test, the correspondences are discarded if the distance between the first and the second nearest neighbors is larger than a manually set threshold. Setting the SNN ratio threshold to 0.8 works well in all our experiments.

5.1. Essential Matrix Estimation

In order to test the essential matrix estimation performance of the proposed algorithm, we downloaded the 13 scenes from the CVPR IMW 2020 PhotoTourism challenge [42]. These scene were also used in the recent CVPR tutorial *RANSAC in 2020* [1] to compare robust estimators. The dataset contains tentative correspondences formed by mutual nearest neighbors matching of RootSIFT descriptors. It also provides SIFT orientations and scales that we can use for training the proposed method. Besides the image matches, the ground-truth intrinsic camera parameters and relative poses are also provided. We use scene St. Peter’s Square, consisting of 4950 image pairs, for training both Deep MAGSAC++ and NG-RANSAC. We use the provided validation set when training the deep learning-based algorithms. For testing, we use 1000 randomly chosen image pairs from each of the remaining 12 scenes. Thus, the methods are tested on a total of 12 000 image pairs.

Before applying the main end-to-end training, we initialize our deep model by minimizing the Kullback–Leibler divergence [49] of the prediction and the target distribution using a 1000-epoch long initial training process. To our experiments, this procedure improves the convergence speed of the end-to-end training. The end-to-end Deep MAGSAC++ framework is trained on the RootSIFT correspondences of St. Peter’s Square (4950 pairs) for 10 epochs, with its inlier-outlier threshold upper bound set to 0.75 pixel, Adam optimizer [25], a batch size of 32, and 10^{-5} learning rate are used.

In each iteration of the training, the pre-filtered correspondences are re-ordered according to the predicted weights and MAGSAC++ is applied to estimate the essential matrix. The network can be trained both in a supervised and self-supervised manner. We report the errors of the model trained in a supervised way where the loss is a combination of the proposed affine loss (Section 3.1), and pose error. For calculating the affine loss, we used the SIFT orientation and scale and the ground truth essential matrix. The pose error is calculated as the maximum of the rotation $\epsilon_{\hat{\mathbf{R}}} = (180/\pi) \cos^{-1} \left(\left(\text{tr} \left(\hat{\mathbf{R}} \mathbf{R}^T \right) - 1 \right) / 2 \right)$, and the angular translation errors, $\epsilon_{\hat{\mathbf{t}}} = (180/\pi) \cos^{-1} \frac{\hat{\mathbf{t}}^T \mathbf{t}}{|\hat{\mathbf{t}}| |\mathbf{t}|}$, in degrees, where $\hat{\mathbf{R}} \in \text{SO}(3)$ is the 3D rotation matrix and $\hat{\mathbf{t}} \in \mathbb{R}^3$ is the translation both decomposed from the estimated essential matrix $\hat{\mathbf{E}}$. Note that we use the angular translation error since the length of $\hat{\mathbf{t}}$ can not be recovered from two views [21]. Also note that the scale and orientations of the features have to be normalized together with the point correspondences by the intrinsic camera matrices \mathbf{K}_1 and \mathbf{K}_2 as proposed in [6]. While the rotation angle remain unchanged, the scale is normalized by f_2/f_1 , where f_i is the focal length of the i th camera, $i \in [1, 2]$.

The network can also be trained in a self-supervised way maximizing the number of inliers. The proposed affine loss

Method	AUC	F1 Score (%)	Median epipolar error	Time (ms)
LMEDS [38]	0.45	38.55	3.15	20
RANSAC [18]	0.78	56.83	0.98	32
GC-RANSAC [7]	0.91	66.90	0.42	56
MAGSAC [11]	0.76	57.80	0.84	233
MAGSAC++ [9]	0.83	60.65	0.75	413
EAS [16]	0.83	55.16	0.88	310
NG-RANSAC [14]	0.92	69.50	0.41	18
Deep MAGSAC++	0.97	69.93	0.29	12

Table 2. The AUC score at 10°, F1 score and median symm. epipolar error (in pixels) on 9690 images pairs from the KITTI dataset.

suits for this scenario as well. However, the supervised version leads to higher accuracy in our experiments.

We adopted the neural network from [14], which comprises 12 residual blocks and several multi-layer perceptions (MLPs). Each block is constructed by two linear layers, a batch normalization layer, and a ReLU activation function [22]. Besides, the global context is included by adding the instance normalization [48] layer into each block. The inlier probabilities of the matches are mapped by a sigmoid function. Finally, MAGSAC++ with the proposed AR-Sampler estimates the essential matrix with its iteration number fixed to 1000. The estimated essential matrix is used to calculate the loss. The number of times each correspondence was selected in a minimal sample is back-propagated and used to update the weights for next iteration.

To measure the accuracy of the estimated essential matrices, we decompose it to rotation and translation and use them to calculate the pose error. Finally, we calculate the AUC score at 5°, 10° and 20° from the pose error as the area under the recall curve [14].

The AUC@10° scores on each scene from the PhotoTourism dataset [42] are reported in Table 1. Also, we show the run-time (in milliseconds) and the AUC scores averaged over all scenes. The proposed Deep MAGSAC++ achieves the highest accuracy on all scenes by a large margin. The second best methods, in terms of accuracy, are MAGSAC, MAGSAC++ and NG-RANSAC with similar scores. Deep MAGSAC++ has a score higher by 9 AUC points on average. Moreover, Deep MAGSAC++ is the second fastest algorithm being just marginally slower than the fastest one, LMEDS, that is significantly less accurate.

The left plot of Fig. 3 shows the cumulative distribution functions (CDF) of the angular pose errors of the estimated essential matrices on all tested scenes. Being accurate is indicated by a curve close to the top-left corner. Deep MAGSAC++ is significantly more accurate than the other compared methods.

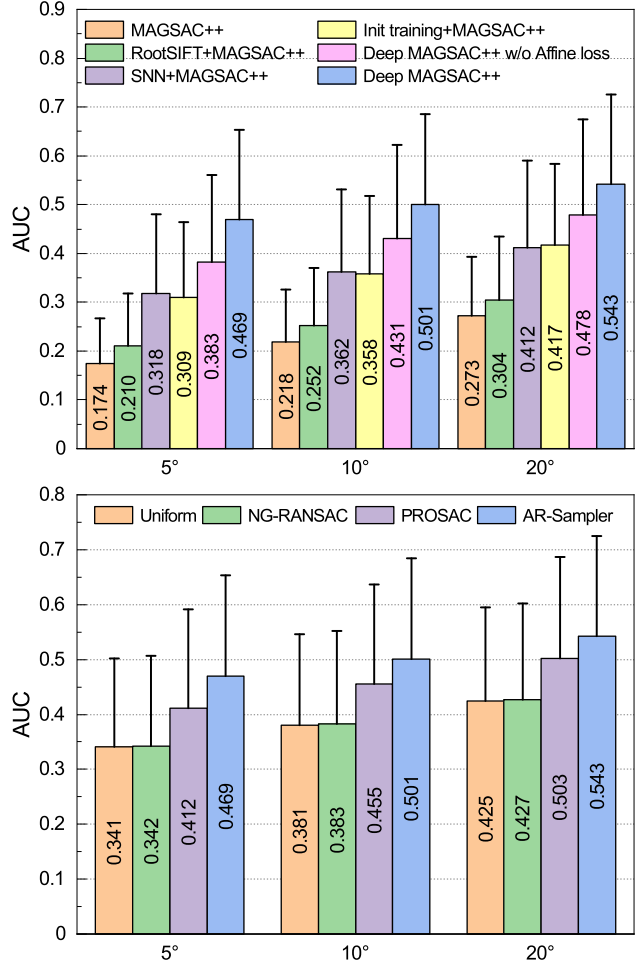


Figure 4. The AUC scores (and their std.) at 5°, 10° and 20° of E estimation on the PhotoTourism dataset [42]. *Top*: the impact of each algorithmic component of Deep MAGSAC++ on the AUC score. *Bottom*: results using the Uniform [17], NG-RANSAC sampler [14], PROSAC [15] and the proposed AR-Sampler.

In the top plot of Fig. 4, we show the accuracy gain from each component of the algorithm. We show the AUC scores and their standard deviations at 5°, 10° and 20°. The results are averaged over the 12 scenes. It can be seen that the proposed affine loss plays an important role in the improved accuracy. Also, it confirms that the widely used techniques, e.g., SNN filtering, RootSIFT, initial training, are important steps to achieve state-of-the-art results.

In the bottom plot of Fig. 4, we show the results of different samplers used within Deep MAGSAC++. The compared samplers are the uniform one from [17], the NG-RANSAC sampler [14], PROSAC [15], and the proposed AR-Sampler. It can be seen that proposed AR-Sampler leads to the best accuracy. Interestingly, PROSAC outperforms significantly the recently proposed sampler of NG-RANSAC which is just marginally more accurate than the

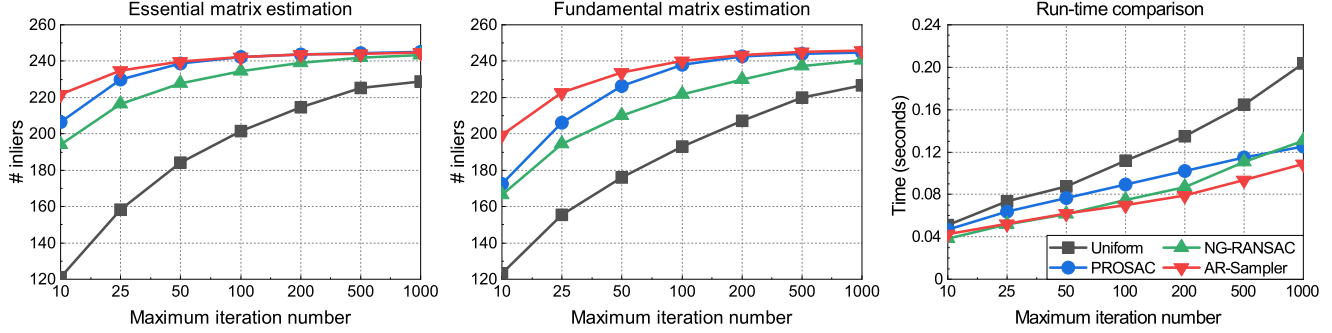


Figure 5. *Left, middle*: the inlier numbers (vertical axis) plotted as a function of the maximum iteration number (horizontal) used in the original MAGSAC++ algorithm [9] when combined with Uniform [17], NG-RANSAC [14], PROSAC [15] and the proposed AR-Sampler. *Right*: the robust estimation time, in seconds, versus the maximum iteration number. The SNN ratio [26] provides the inlier probabilities.

uniform sampler when used inside Deep MAGSAC++.

5.2. Fundamental Matrix Estimation

We evaluate Deep MAGSAC++ for fundamental matrix estimation on the KITTI benchmark [19]. As in [14, 51], Sequences '00-05' and '06-10' are regarded as the training and testing sets, respectively. The KITTI dataset consists of consecutive frames of high-resolution cameras mounted to moving vehicle in a mid-size city, rural areas and highways [19]. The images are of resolution 1226×370 . Image correspondences are detected between subsequent images by RootSIFT. In total, we use 14 130 image pairs from KITTI for training, and another 9060 for testing.

Fundamental matrix estimation runs on the same architecture as what we described in Section 5.1. In this case, neither the point coordinates, nor the orientation and scale are normalized. In contrast to essential matrix estimation, we do apply initial training as it does not improve the accuracy when estimating fundamental matrices.

Table 2 reports the run-time, the median sym. epipolar error in pixels, the AUC and F1 scores of the estimated fundamental matrices compared to the ground truth. Deep MAGSAC++ leads to the highest accuracy in all metrics. Interestingly, while F1 score is only marginally higher than that of NG-RANSAC, the AUC score is better by 5%. This implies that the F1 score is not in perfect agreement with the actual camera pose error captured in the AUC score. The run-time of Deep MAGSAC++ is the lowest, being 33% faster than the second one, *i.e.*, NG-RANSAC. These timings exclude the prediction time which is at most a 1-2 milliseconds. Fig. 3 shows the CDFs of the epipolar errors (middle) and the F1 scores (right) on the 9060 image pairs. Deep MAGSAC++ leads to the best errors and F1 score.

5.3. Sampler Comparison

We test the proposed sampler on the 4950 image pairs from scene Sacre Coeur when using the standard second nearest neighbor (SNN) ratio to order the points according

to the inlier probabilities. To our experiments, considering the SNN ratio directly as prior inlier probability does not lead to an improvement compared to PROSAC. However, exploiting the point ranks implied by the SNN ratio works well. Assume that we are given n points $\mathbf{p}_{i_1}, \dots, \mathbf{p}_{i_n}$ ordered by their SNN ratios s_{i_1}, \dots, s_{i_n} . Thus, $s_{i_1} \leq s_{i_2} \leq \dots \leq s_{i_n}$. We calculate the prior probability of the i_j th point as $\mu_{i_j} = 1 - (j - 1)/(n - 1)$, $j \in [1, n]$. Consequently, the first point when ordered by the SNN ratio has 1 as prior probability. Conversely, the last one is assigned 0.

The inlier numbers and run-times of the original MAGSAC++ when used together with the uniform [17], PROSAC [15], NG-RANSAC samplers [14], and the proposed one are shown in Fig. 5. The horizontal axis is the maximum iteration number which is a strict upper bound on the iteration number that is controlled by the RANSAC confidence parameter. The curve of the proposed sampler starts from a higher inlier number, both for \mathbf{F} and \mathbf{E} estimation, than that of the others, *i.e.*, it leads to finding good samples earlier than the other methods. As expected, after many iterations, all methods converge to the similar results. Due to being extremely efficient, AR-Sampler leads to the fastest robust estimation as shown in the right plot of Fig. 5.

6. Conclusion

In this paper, we propose the Deep MAGSAC++ algorithm that achieves state-of-the-art accuracy while having comparable or better processing time to its less accurate alternatives. It runs in *real-time* on most of the tested problems. Moreover, we show that exploiting additional geometric information in the loss function helps in capturing the underlying scene geometry. This extra information is available *for free* when using partially affine covariant feature detectors, *e.g.*, SIFT. The proposed AR-Sampler is superior to the traditional ones both when using predicted weights or SNN ratios as inlier probabilities.

References

- [1] Ransac tutorial 2020- data. <https://github.com/ducha-aiki/ransac-tutorial-2020-data>. 6
- [2] Relja Arandjelović and Andrew Zisserman. Three things everyone should know to improve object retrieval. In *2012 IEEE Conference on Computer Vision and Pattern Recognition*, pages 2911–2918. IEEE, 2012. 6
- [3] Daniel Barath. Five-point fundamental matrix estimation for uncalibrated cameras. pages 235–243, 2018. 3, 4
- [4] D. Barath, T-J. Chin, O. Chum, D. Mishkin, R. Ranftl, and J. Matas. RANSAC in 2020 tutorial. In *Conference on Computer Vision and Pattern Recognition*, 2020. 2
- [5] Daniel Barath and Levente Hajder. Efficient recovery of essential matrix from two affine correspondences. *IEEE Transactions on Image Processing*, 27(11):5328–5337, 2018. 3
- [6] Daniel Barath and Zuzana Kukelova. Homography from two orientation-and scale-covariant features. In *Proceedings of the IEEE/CVF International Conference on Computer Vision*, pages 1091–1099, 2019. 6
- [7] Daniel Barath and Jiří Matas. Graph-cut RANSAC. In *Conference on Computer Vision and Pattern Recognition*, pages 6733–6741, 2018. 5, 7
- [8] Daniel Barath and Jiri Matas. Progressive-X: Efficient, anytime, multi-model fitting algorithm. In *Proceedings of the IEEE/CVF International Conference on Computer Vision*, pages 3780–3788, 2019. 1
- [9] Daniel Barath, Jana Noskova, Maksym Ivashechkin, and Jiri Matas. MAGSAC++, a fast, reliable and accurate robust estimator. In *Conference on Computer Vision and Pattern Recognition*, 2020. 1, 2, 5, 7, 8
- [10] Daniel Barath, Jana Noskova, Maksym Ivashechkin, and Jiri Matas. Magsac++, a fast, reliable and accurate robust estimator. In *Proceedings of the IEEE/CVF conference on computer vision and pattern recognition*, pages 1304–1312, 2020. 2
- [11] Daniel Barath, Jana Noskova, and Jiří Matas. MAGSAC: marginalizing sample consensus. In *Conference on Computer Vision and Pattern Recognition*, 2019. <https://github.com/danini/magsac>. 5, 7
- [12] Daniel Barath, Jana Noskova, and Jiri Matas. Marginalizing sample consensus. *IEEE Transactions on Pattern Analysis and Machine Intelligence*, 2021. 5, 6
- [13] Herbert Bay, Tinne Tuytelaars, and Luc Van Gool. SURF: Speeded up robust features. In *European conference on computer vision*, pages 404–417. Springer, 2006. 3
- [14] Eric Brachmann and Carsten Rother. Neural-guided ransac: Learning where to sample model hypotheses. pages 4322–4331, 2019. 2, 3, 5, 7, 8
- [15] O. Chum and J. Matas. Matching with PROSAC-progressive sample consensus. In *Conference on Computer Vision and Pattern Recognition*. IEEE, 2005. 2, 3, 7, 8
- [16] Aoxiang Fan, Jiayi Ma, Xingyu Jiang, and Haibin Ling. Efficient deterministic search with robust loss functions for geometric model fitting. *IEEE Transactions on Pattern Analysis and Machine Intelligence*, 2021. 5, 7
- [17] M. A. Fischler and R. C. Bolles. Random sample consensus: a paradigm for model fitting with applications to image analysis and automated cartography. *Communications of the ACM*, 1981. 1, 5, 7, 8
- [18] Martin A. Fischler and Robert C. Bolles. Random sample consensus: A paradigm for model fitting with applications to image analysis and automated cartography. *Commun. ACM*, 24(6):381–395, June 1981. 5, 7
- [19] Andreas Geiger, Philip Lenz, and Raquel Urtasun. Are we ready for autonomous driving? the KITTI vision benchmark suite. In *Conference on Computer Vision and Pattern Recognition*. IEEE, 2012. 1, 6, 8
- [20] D. Ghosh and N. Kaabouch. A survey on image mosaicking techniques. *Journal of Visual Communication and Image Representation*, 2016. 1
- [21] R. Hartley and A. Zisserman. *Multiple view geometry in computer vision*. Cambridge university press, 2003. 6
- [22] Kaiming He, Xiangyu Zhang, Shaoqing Ren, and Jian Sun. Delving deep into rectifiers: Surpassing human-level performance on imagenet classification. In *Proceedings of the IEEE international conference on computer vision*, pages 1026–1034, 2015. 7
- [23] Sergey Ioffe and Christian Szegedy. Batch normalization: Accelerating deep network training by reducing internal covariate shift. In Francis Bach and David Blei, editors, *Proceedings of the 32nd International Conference on Machine Learning*, volume 37 of *Proceedings of Machine Learning Research*, pages 448–456, Lille, France, 07–09 Jul 2015. PMLR. 2
- [24] H. Isack and Y. Boykov. Energy-based geometric multi-model fitting. *IJCV*, 2012. 1
- [25] Diederik P Kingma and Jimmy Ba. Adam: A method for stochastic optimization. *arXiv preprint arXiv:1412.6980*, 2014. 6
- [26] D. G. Lowe. Object recognition from local scale-invariant features. In *International Conference on Computer Vision*. IEEE, 1999. 2, 3, 4, 6, 8
- [27] Jiayi Ma, Xingyu Jiang, Aoxiang Fan, Junjun Jiang, and Junchi Yan. Image matching from handcrafted to deep features: A survey. *IJCV*, 129(1):23–79, 2021. 2
- [28] Ricardo A Maronna, R Douglas Martin, Victor J Yohai, and Matías Salibián-Barrera. *Robust statistics: theory and methods (with R)*. John Wiley & Sons, 2019. 2
- [29] J. Matas, O. Chum, M. Urban, and T. Pajdla. Robust wide-baseline stereo from maximally stable extremal regions. *IVC*, 2004. 1
- [30] Krystian Mikolajczyk, Tinne Tuytelaars, Cordelia Schmid, Andrew Zisserman, Jiri Matas, Frederik Schaffalitzky, Timor Kadir, and Luc Van Gool. A comparison of affine region detectors. *International journal of computer vision*, 65(1):43–72, 2005. 3
- [31] Dmytro Mishkin, Jiri Matas, and Michal Perdoch. MODS: Fast and robust method for two-view matching. *Computer Vision and Image Understanding*, 141:81–93, 2015. 1, 3
- [32] Kai Ni, Hailin Jin, and Frank Dellaert. GroupSAC: Efficient consensus in the presence of groupings. In *International Conference on Computer Vision*, pages 2193–2200. IEEE, 2009. 2
- [33] T. T. Pham, T-J. Chin, K. Schindler, and D. Suter. Interacting geometric priors for robust multimodel fitting. *TIP*, 2014. 1

- [34] P. Pritchett and A. Zisserman. Wide baseline stereo matching. In *International Conference on Computer Vision*. IEEE, 1998. 1
- [35] Rene Ranftl and Vladlen Koltun. Deep fundamental matrix estimation. In *ECCV*, 2018. 2
- [36] Carolina Raposo and Joao P Barreto. Theory and practice of structure-from-motion using affine correspondences. pages 5470–5478, 2016. 3
- [37] Peter J Rousseeuw. Least median of squares regression. *Journal of the American statistical association*, 79(388):871–880, 1984. 5
- [38] Peter J Rousseeuw and Annick M Leroy. *Robust regression and outlier detection*, volume 589. John wiley & sons, 2005. 5, 7
- [39] Ethan Rublee, Vincent Rabaud, Kurt Konolige, and Gary Bradski. ORB: An efficient alternative to SIFT or SURF. pages 2564–2571. Ieee, 2011. 3
- [40] Johannes Lutz Schönberger and Jan-Michael Frahm. Structure-from-motion revisited. In *Conference on Computer Vision and Pattern Recognition*, 2016. 1
- [41] Johannes Lutz Schönberger, Enliang Zheng, Marc Pollefeys, and Jan-Michael Frahm. Pixelwise view selection for unstructured multi-view stereo. In *European Conference on Computer Vision*, 2016. 1
- [42] Noah Snavely, Steven M Seitz, and Richard Szeliski. Photo tourism: exploring photo collections in 3d. In *ACM siggraph 2006 papers*, pages 835–846. 2006. 1, 5, 6, 7
- [43] Weiwei Sun, Wei Jiang, Andrea Tagliasacchi, Eduard Trulls, and Kwang Moo Yi. Attentive context normalization for robust permutation-equivariant learning. 2020. 2
- [44] Philip Hilaire Torr, Slawomir J Nasuto, and John Mark Bishop. NAPSAC: High noise, high dimensional robust estimation-it’s in the bag. 2002. 2
- [45] P. H. S. Torr and D. W. Murray. Outlier detection and motion segmentation. In *Optical Tools for Manufacturing and Advanced Automation*. International Society for Optics and Photonics, 1993. 1
- [46] P. H. S. Torr and A. Zisserman. MLESAC: A new robust estimator with application to estimating image geometry. *CVIU*, 2000. 1
- [47] P. H. S. Torr, A. Zisserman, and S. J. Maybank. Robust detection of degenerate configurations while estimating the fundamental matrix. *CVIU*, 1998. 1
- [48] Dmitry Ulyanov, Andrea Vedaldi, and Victor Lempitsky. Instance normalization: The missing ingredient for fast stylization. *arXiv preprint arXiv:1607.08022*, 2016. 7
- [49] Tim Van Erven and Peter Harremos. Rényi divergence and kullback-leibler divergence. *IEEE Transactions on Information Theory*, 60(7):3797–3820, 2014. 6
- [50] Kwang Moo Yi*, Eduard Trulls*, Yuki Ono, Vincent Lepetit, Mathieu Salzmann, and Pascal Fua. Learning to find good correspondences. 2018. 2
- [51] Kwang Moo Yi, Eduard Trulls, Yuki Ono, Vincent Lepetit, Mathieu Salzmann, and Pascal Fua. Learning to find good correspondences. In *Proceedings of the IEEE conference on computer vision and pattern recognition*, pages 2666–2674, 2018. 5, 8
- [52] Jiahui Zhang, Dawei Sun, Zixin Luo, Anbang Yao, Lei Zhou, Tianwei Shen, Yurong Chen, Long Quan, and Honggen Liao. Learning two-view correspondences and geometry using order-aware network. 2019. 2
- [53] Chen Zhao, Yixiao Ge, Feng Zhu, Rui Zhao, Hongsheng Li, and Mathieu Salzmann. Progressive correspondence pruning by consensus learning. 2021. 2, 6
- [54] M. Zuliani, C. S. Kenney, and B. S. Manjunath. The multi-RANSAC algorithm and its application to detect planar homographies. In *ICIP*. IEEE, 2005. 1